Revisiting equivalent optical properties for cerebrospinal fluid to improve diffusion-based modeling accuracy in the brain

Aiden Vincent Lewis[a], **and Qianqian Fang**[a,b,*]
[a]Northeastern University, Department of Bioengineering, 360 Huntington Avenue, Boston, USA, 02115
[b]Northeastern University, Department of EECS, 360 Huntington Avenue, Boston, USA, 02115

Abstract.
Significance: The diffusion approximation (DA) is used in functional near-infrared spectroscopy (fNIRS) studies despite its known limitations due to the presence of cerebrospinal fluid (CSF). Nearly all of these studies rely on a set of empirical CSF optical properties, recommended by a previous simulation study, that were not selected for the purpose of minimizing DA modeling errors.
Aim: We aim to directly quantify the accuracy of DA solutions in brain models by comparing those with the gold-standard solutions produced by the mesh-based Monte Carlo (MMC), based on which we derive updated recommendations.
Approach: For both a 5-layer head and Colin27 atlas models, we obtain DA solutions by independently sweeping the CSF absorption (μ_a) and reduced scattering (μ_s') coefficients. Using an MMC solution with literature CSF optical properties as reference, we compute the errors for surface fluence, total brain sensitivity and brain energy-deposition, and identify the optimized settings where the such error is minimized.
Results: Our results suggest that previously recommended CSF properties can cause significant errors (8.7% to 52%) in multiple tested metrics. By simultaneously sweeping μ_a and μ_s', we can identify infinite numbers of solutions that can exactly match DA with MMC solutions for any single tested metric. Furthermore, it is also possible to simultaneously minimize multiple metrics at multiple source/detector separations, leading to our new recommendation of setting $\mu_s' = 0.15$ mm^{-1} while maintaining physiological μ_a for CSF in DA simulations.
Conclusion: Our new recommendation of CSF equivalent optical properties can greatly reduce the model mismatches between DA and MMC solutions at multiple metrics without sacrificing computational speed. We also show that it is possible to eliminate such a mismatch for a single or a pair of metrics of interest.

Keywords: fNIRS, Cerebrospinal fluid, Monte Carlo simulations, Diffusion approximation, Brain imaging, Photobiomodulation.

*Qianqian Fang, q.fang@neu.edu

1 Introduction

In the wavelength range between 600 nm and 1,100 nm, near-infrared (NIR) light can penetrate several centimeters of biological tissues with a highly scattering trajectory, as a result of relatively low tissue absorption. Multiple imaging techniques, such as functional near infrared spectroscopy (fNIRS) and diffuse optical tomography (DOT), capitalize upon this behavior to non-invasively monitor hemodynamics in cortical tissue resulting from brain activities. Similarly, in photobiomodulation (PBM) applications, clinicians use this phenomenon to deliver light to deep

tissues for therapeutic purposes. Due to the highly scattering and stochastic nature of light-tissue interactions, researchers rely on quantitative modeling techniques to predict light dosages and analyze their measurements. Two widely used numerical techniques for quantitatively modeling light-tissue-interactions are the diffusion approximation (DA)[1] and the Monte Carlo (MC) method.[2]

MC is a stochastic solver to the radiative transfer equation (RTE), a differential-integral equation known to be accurate for modeling light transport in general random media including biological tissues. MC is also relatively easy to implement and can be easily parallelized. However, the primary challenge MC faces is its high computational cost, as it requires to launch large numbers of photon packets to achieve a stable solution with acceptable stochastic noise. Over the past two decades, the widespread use of graphics processing units (GPU) has drastically reduced MC modeling time from several hours[3] to tens of seconds.[4] MC-based models have also been extended to accommodate increasingly complex tissue shapes, growing from infinite layered media[5] to spatially heterogeneous voxel-based,[3,6] mesh-based[7] or hybrid shape representations.[8,9] As a result, MC solutions have been increasingly seen in routine data analysis aside from serving its transitional role of providing gold-standard solutions.[10]

In comparison, DA solves a simplified version of the RTE by ignoring the ballistic behaviors of photons near a collimated source or in void/low-scattering regions. This results in a simpler elliptic partial different equation (PDE) that can be conveniently solved using numerical techniques such as finite-element (FE) or finite-difference (FD) methods. Typical solution time for a DA forward solution using an FE solver, such as NIRFAST[11] or Redbird,[12] is on the scale of a fraction of a second. This is significantly faster than MC solutions, even with GPU accelerations, and the output is deterministic (i.e. free of stochastic noise). Because of the high computational efficiency, the DA has been actively used in DOT image reconstructions especially when arrays of sources

and detectors are used. However, when modeling light transport in the brain, a number of previous studies had demonstrated that the presence of low-scattering tissues such as cerebrospinal fluid (CSF) can produce erroneous solutions.[13–18] A number of hybrid methods have been proposed to properly model voids and low-scattering tissues, such as CSF, lung, synovial fluid, cysts etc, however, these methods have received only limited adoption due to increased complexity.

The CSF layer is generally known to have low scattering, however, its literature absorption (μ_a) and reduced scattering coefficients (μ_s') show a wide range of values, ranging between 0.0004 mm^{-1} and 0.004 mm^{-1} for μ_a,[19,20] and between 0.001 mm^{-1} and 3.0 mm^{-1} for μ_s'[10,21] due to diverse measurement methods and modeling assumptions. The CSF layer also occupies a complex anatomical space, filling primarily the subarachnoid space bounded by the arachnoid mater at the outer surface and the pia mater at the inner surface,[22] as well as the folding space on the cerebrum surface, known as sulci. The CSF in the sulci are predominantly transparent, filling a complex folding geometry. Sulci's widths and depths are highly dependent on locations, ranging from 0.2 to 2.3 mm for width and 5.7 to 13 mm for depth in young adults, varying further between age groups and genders.[22] Multiple approaches for modeling CSF in the brain exist, including treating it entirely as a translucent fluid,[20,21] assigning separate optical properties to the subarachnoid space and sulci,[10] and combining it with the cortical tissue using empirically derived bulk properties.[23]

A widely cited approach for extending DA in modeling light transport in the brain is described by Custo *et al.*[20] In this work, the CSF layer is treated entirely as a diffusive medium with a recommended empirical reduced scattering coefficient of 0.3 mm^{-1} – determined by the typical inverse line-of-sight distance of the CSF layer.[20] Because of the simplicity, this recommmendation has been widely adopted to justify the use of DA in modeling the CSF in the brain tissues.[24,25] Diffusion solvers such as NIRFAST[11] and NeuroDOT[26] also include this recommended CSF scattering

property in many built-in examples for brain related data analyses, and received wide adoption among fNIRS research.[27–29] However, most of the works utilizing this approach took the recommended values as the optimal solution without further scrutinizing the limitations on how such a recommendation was derived.

We want to highlight that it is particularly important to understand the conditions upon which the recommended CSF optical properties in Custo *et al.* were derived. First of all, this recommendation was drawn entirely based on comparing between MC solutions at varying CSF reduced scattering coefficients, instead of directly comparing between MC and DA solutions. Secondly, the chosen value $\mu_s' = 0.3$ mm^{-1} was determined as the upper-bound beyond which the MC solutions start to show large deviations from the respective ground-truth simulations; this "upper-bound" criterion was also quite different from the "optimal value" that best approximates DA with MC in the CSF that most use-cases of this recommendation commonly assumed. Thirdly, the physical quantity studied in the previous work is specifically limited to fluence and partial-path-lengths; the impact to other types of optical measurements, such as brain sensitivity – desired when solving fNIRS brain activity recovery and image reconstructions – and energy deposition – desired in many PBM related analyses – were not discussed. Lastly, the previous work only examined the impact of varying μ_s'; the impact of simultaneously altering CSF absorption coefficient μ_a was not considered.

Here, we would like to revisit this widely adopted recommendation by addressing the aforementioned limitations. Specifically, we aim to directly compare DA with MC solutions and seek to derive more appropriate CSF equivalent optical properties based on minimizing their differences. In addition to sweeping its reduced scattering coefficient, we also allow the CSF's absorption coefficient to change, adding a new degree-of-freedom to help reduce the model mismatch. Moreover,

we expand the comparison between DA and MC to include total brain sensitivity and energy deposition, extending the new recommendation towards broader optical brain imaging/therapy techniques. Furthermore, we compare our DA and MC solutions on both a simplified 5-layered head model as well as a more complex adult brain atlas – Colin27 [30] – at two common wavelengths, seeking further generalization of our findings. Here we use our extensively developed mesh-based MC (MMC), known for its high accuracy among various MC solvers,[7] with graphics processing unit (GPU) acceleration[4] to provide the reference solution. To further remove the confounding systematic differences due to varying spatial discretization, we apply an identical set of tetrahedral meshes for use in both the FE DA solver and MMC.

In the remainder of this paper, we present our methodologies and results for minimizing DA modeling errors comparing to results obtained from MC. First, we describe the layered head and atlas anatomical models used, as well as the numerical solvers used for DA and MC respectively. Then, we describe the metrics we derive from the DA and MC solutions, such as brain sensitivity, surface fluence, and GM energy deposition; these metrics are used to quantify the errors caused by using DA in fNIRS and PBM applications. Finally, we discuss the results from both the layered and brain-atlas models, demonstrating that use of updated optical properties for CSF in DA models can significantly reduce, or even eliminate, mismatch against the "gold standard" MC models.

2 Methods

2.1 Anatomical models and tetrahedral mesh generation

We perform MC and DA simulations of light transport in two brain anatomical models frequently seen in literature: 1) a 5-layer head model and 2) Colin27 brain atlas.[31] The 5-layered head model is created with layer thicknesses based on the average thickness of the atlas layers.[31] Note that

	Skull/Scalp[19]		Cerebrospinal fluid[19,20]		Gray matter[32]		White matter[32]	
Properties (mm^{-1})	μ_a	μ_s'	μ_a	μ_s'	μ_a	μ_s'	μ_a	μ_s'
690 nm	0.0159	1.00	0.0004	0.001	0.02	0.88	0.07	6.00
830 nm	0.0191	0.86	0.0026	0.001	0.03	0.70	0.09	4.29

Table 1 Assumed absorption (μ_a) and reduced scattering coefficients (μ_s'), both in mm^{-1}, based upon literature used to obtain the ground-truth results using Monte Carlo simulations.

the scalp and skull are treated with one set of optical properties as in literature.[31] A tetrahedral mesh of the Colin27 atlas is generated using the Brain2Mesh toolbox[31] and is derived from the Colin27 magnetic resonance imaging (MRI) atlas, with four layers: combined scalp and skull, CSF, gray matter (GM), and white matter (WM). The physiological values for each layer, used in MC simulations serving as the ground-truth, are described in Table 1. We want to note here that all simulations in Custo *et al.*[20] used an assumed CSF μ_a value of 0.004 mm^{-1}. However, this value is 10$\times$ larger than the physiological μ_a value of 0.0004 mm^{-1} reported in Strangman *et al.*,[19] which was also cited as the source of the optical properties. For consistency in the rest of our analysis, we use the μ_a values from the upstream source of Strangman *et al.*[19] in all our reference simulations.

2.2 Forward models

We use our GPU-accelerated, mesh-based Monte Carlo (MMC) photon transport simulator[4] – an open-source software that has been widely validated and disseminated among the biophotonics community[33–38] – to create the "ground-truth" solutions. Briefly, MMC uses tetrahedral meshes to produce MC simulations calculating fluence at every node[7] or element. The use of tetrahedral meshes allows simulations to consider more realistic biological tissues with curved and complex boundaries. All MC solutions are produced with a relatively large number (10^9) of photon packets to ensure stable results. For DA, we apply another in-house MATLAB toolbox named "Redbird-m" to provide diffusion solutions using a finite-element method (FEM).[12] Redbird-m was developed

from our various previous works, extending from optical breast imaging[39] and structural-prior guided reconstructions.[40,41] To properly approximate a collimated source, such as a coupling fiber used in fNIRS probes, in Redbird-m, we sink both sources and detectors by $1/\mu_s'$ from the tissue-air boundary along the light incident direction.[42]

In all simulations reported below, both MMC and Redbird-m produce solutions over the same tetrahedral mesh generated by our Iso2Mesh mesh generator.[31] This allows us to minimize discrepancies due to different discretization strategies. In addition, both solvers have implemented normalization methods to produce solutions that correspond to the Green's function of the respective mathematical models, therefore, they can be directly compared at all nodal positions.

To simulate a typical fNIRS probe configuration, a pencil beam source is placed on the top surface of the chosen head model; a linear array of disk-shaped detectors with a radius of 1.5 mm, with a geodesic distance to the source ranging between 2.0 cm to 3.5 cm with an increment of 0.5 cm, are placed on one or both sides of the source. An additional near-separation detector was placed at a 0.84 cm geodesic distance from the source.

2.3 Metrics for accuracy assessments

To quantify the mismatch between MC and DA, we compute common metrics relevant to evaluating performance in PBM and fNIRS applications. For PBM, the total energy deposition within the GM layer (E_{gm}) is computed to characterize the dosage of light energy that reaches the brain for therapeutic usage. For fNIRS, multiple metrics are used: 1) spatially resolved fluence, $\Phi(\vec{r})$, and detected fluence values, $\Phi(\vec{r}_s, \vec{r}_d)$, sampled at detector locations ($\vec{r}_d$) for any given source at r_s are extracted to assess the similarity of optical measurements between MC and DA,[13] 2) the spatially resolved μ_a Jacobian, $J(\vec{r})$, i.e. sensitivity of μ_a at each location ($\vec{r}$), is computed to assess the loss

of sensitivity caused by using DA,[43] 3) the total brain sensitivity (S_{gm}), computed by summing the Jacobian within the GM region, to estimate the overall impact of forward model accuracy to the recovery of brain hemodynamics, and finally, 4) fraction of GM sensitivity over total sensitivity (F_{gm}) is used to quantify the relative impact of the forward models to fNIRS signal recovery. The definitions of each of the above metrics are detailed below.

In each of the used head models, a forward solution is produced using MMC and Redbird-m, respectively, by placing a pencil beam over the source position, with an incident direction along the normal direction of the surface. Both MC and DA simulations produce forward solutions of normalized fluence, Φ, as a Green's function defined at each spatial location $\vec{r} \in \Omega$ where Ω denotes the simulated domain. To calculate the total energy deposition to the brain, E_{gm}, an integral of the forward fluence solution, $\Phi(\vec{r}, \vec{r}_s)$, multiplied by $\mu_a(\vec{r})$ is performed within the GM region, Ω_{gm}.

$$E_{gm} = \int_{\vec{r} \in \Omega_{gm}} \Phi(\vec{r}, \vec{r}_s) \mu_a(\vec{r}) d\vec{r} \tag{1}$$

To calculate the fluence at various detectors, $\Phi(\vec{r}_d, \vec{r}_s)$, a simple linear interpolation is applied to obtain the normalized fluence at the exact coordinate $\vec{r}_d$ of the detector based on the forward fluence solution $\Phi(\vec{r}, \vec{r}_s)$ within the enclosing tetrahedron.

We apply the adjoint method[1,44] to compute the Jacobian matrix in both DA and MC. This is done by multiplying the forward solution simulated from the source, $\Phi(\vec{r}, \vec{r}_s)$, by an adjoint solution, $\Phi(\vec{r}, \vec{r}_d)$, obtained by simulating a source at the location of the detector $\vec{r}_d$. To compute the total brain sensitivity, S_{gm}, we integrate the spatially resolved Jacobian over the entire GM region as

$$S_{gm} = -\int_{\vec{r} \in \Omega_{gm}} \frac{\Phi(\vec{r}, \vec{r}_s)\Phi(\vec{r}, \vec{r}_d)}{\Phi(\vec{r}_d, \vec{r}_s)} d\vec{r}. \tag{2}$$

Finally, we derive the fraction of Jacobian sensitivity over the total sensitivity, F_{gm}, by taking a ratio of the total brain sensitivity over the Jacobian integrated through the entire head model Ω as

$$F_{gm} = \frac{S_{gm}}{-\int_{\vec{r}\in\Omega} \frac{\Phi(\vec{r},\vec{r}_s)\Phi(\vec{r},\vec{r}_d)}{\Phi(\vec{r}_d,\vec{r}_s)} d\vec{r}}. \tag{3}$$

For each of the above metrics (M), a signed percentage error of DA relative to MC is computed as

$$\epsilon_{DA} = \frac{(M_{DA} - M_{MC})}{M_{MC}} \times 100\%, \tag{4}$$

where $\epsilon_{DA} < 0$ represents a case where DA underestimates the ground truth, and $\epsilon_{DA} > 0$ represents overestimation.

3 Results

A tetrahedral mesh of 332,430 nodes and 2,015,332 elements is created using Iso2Mesh for the 5-layered head model; another tetrahedral mesh containing 151,097 nodes and 930,046 elements is produced for the Colin27 atlas. Both mesh models are shared between the MMC and Redbird-m solvers. All MMC simulations are launched using an NVIDIA RTX 2080 SUPER GPU on a Ubuntu 20.04 Linux server. DA solutions computed using Redbird-m are obtained using an AMD Threadripper 3990X processor on the same server.

3.1 Assessing accuracy of diffusion approximations using literature recommendations

Cross-sectional contour plots across all source and detector positions are shown in Fig. 1 comparing DA with the respective MC reference solutions at various conditions. In Figs. 1(a) and 1(d), we artificially set the CSF to a diffusive medium of $\mu_a = 0.0026$ mm^{-1} and $\mu_s' = 1$ mm^{-1} with a

goal of validating Redbird-m DA solver against the reference MMC solutions. With no surprise, the Redbird-m and MMC solutions are closely aligned across the entire simulation domain in both tested head models. The excellent agreement is also indicated by the relatively uniform and low relative errors (color shade) in most of the brain regions. In Figs. 1(b) and 1(e), we set the CSF to the anticipated physiological values ($\mu_a = 0.0026$ mm^{-1}, $\mu_s' = 0.001$ mm^{-1}).[19,20] The significantly elevated errors in CSF, GM and WM layers as well as at larger source-detector separations once again verify the inability of DA to model low-scattering tissues directly.

In Figs. 1(c) and 1(f), we set the CSF's optical properties to $\mu_a = 0.0026$ mm^{-1} and $\mu_s' = 0.3$ mm^{-1}) as recommended by Custo *et al.*[20] It is clear from these results that this approach significantly reduces the overall mismatch between DA and MC. However, notable spatially-resolved errors ranging between 10% to 50% can still be observed within the CSF, GM and WM regions, as well as in large source-detector separations.

3.2 Optimization of optical properties in a 5-layer head model

To identify the optimal CSF equivalent optical properties for approximating MC simulations, in this section, we compute the DA forward solutions by sweeping CSF absorption (μ_a) and reduced scattering coefficient (μ_s') in a large search space that encompasses the typical values seen in biological tissues. The search space for μ_a ranges between 0 mm^{-1} and 0.04 mm^{-1} with a step size of 0.002 mm^{-1}; that for μ_s' ranges between 0 mm^{-1} and 0.4 mm^{-1} in increments of 0.02 mm^{-1}. The only exception is at $\mu_a = \mu_s' = 0$ mm^{-1}, where we had to set μ_s' to a small value (0.001 mm^{-1}) to allow the DA solver to produce valid solutions.

The signed errors (ϵ_{DA}) for E_{gm}, Φ, S_{gm} and F_{gm} as defined in Section 2.3, at a source-detector separation of 35 mm, are computed and plotted in Figs. 2(a) to 2(d), respectively. The color

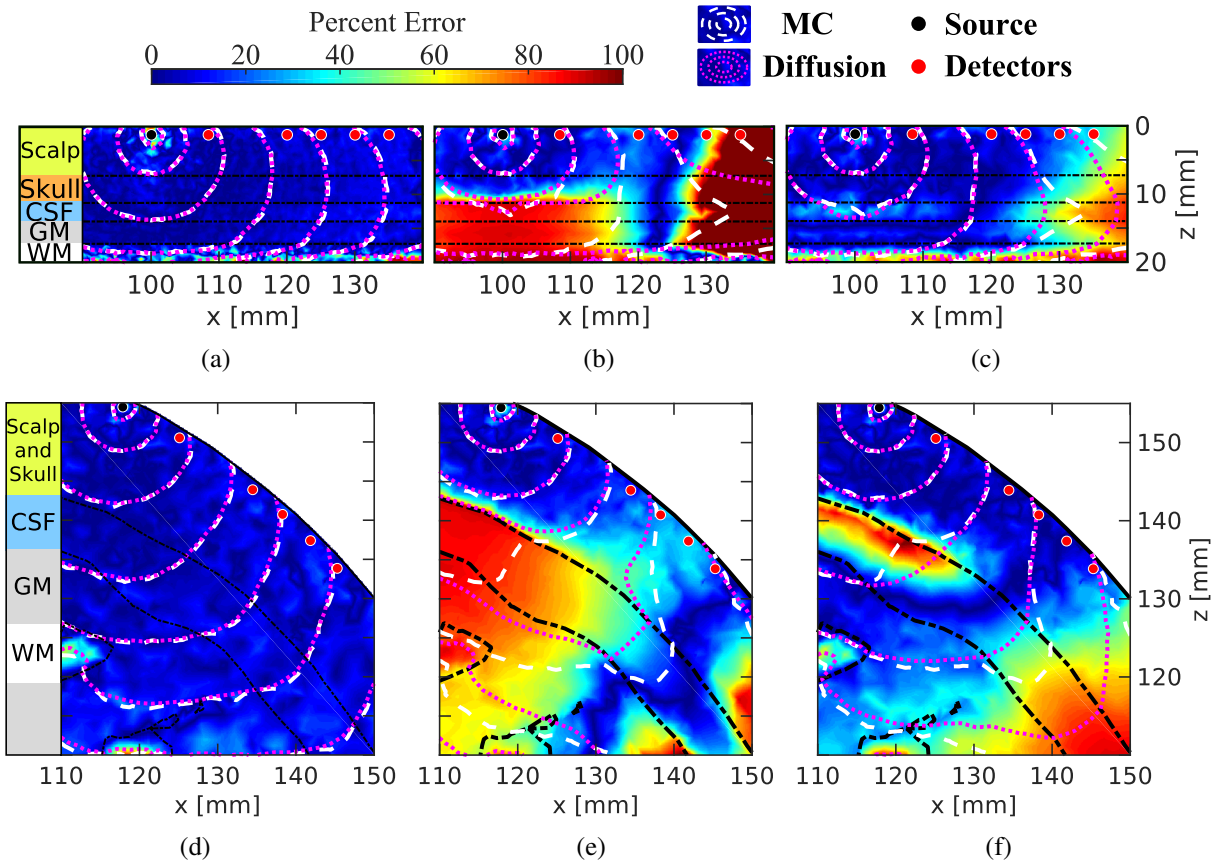

Fig 1 Comparison between diffusion approximation (DA) and Monte Carlo (MC) models in fluence distributions (contour lines) and percentage errors (color maps) in (a-c) a 5-layered head model and (d-f) the Colin27 atlas with a 830 nm source. The cerebrospinal fluid (CSF) optical properties are set to (a, d) a non-physiological diffusive medium of $\mu_a = 0.0026$ mm^{-1} and $\mu_s' = 1$ mm^{-1}, (b, e) the assumed physiological values of $\mu_a = 0.0026$ mm^{-1}, $\mu_s' = 0.001$ mm^{-1}, and (c, f) the literature recommended equivalent values for DA at $\mu_a = 0.0026$ mm^{-1} and $\mu_s' = 0.3$ mm^{-1}) while MC utilizes CSF's physiological values.

scales of all error contour plots are normalized to be between -100% and 100%, with positive errors (where DA overestimates the metric compared to MC) are shown in red and negative errors (where DA underestimates MC) are shown in blue. A red-colored square indicates the literature recommended value at $\mu_a = 0.0026$ mm^{-1} and $\mu_s' = 0.3$ mm^{-1}. A star is used to mark the physiological value that we used to run the MC simulation. A dashed line is plotted on each panel indicating the "zero-error contour" line where DA estimates exactly match those from MC (i.e. no error). Based on these plots, we found that the literature recommended CSF optical properties can result in -8.7% error in E_{gm}, -35% error in Φ, -48% error in S_{gm} and -52% error in F_{gm} (negative errors suggest that DA underestimates MC solutions).

We want to highlight that, for any of the given metrics, it is possible to perfectly match DA with MC values, thanks to the extra degree-of-freedom when allowing both μ_a and μ_s' to vary simultaneously. In fact, there are an infinite number of such solutions, indicated by the continuous zero-error contour line. In other words, every combination of μ_a and μ_s' values along this line would allow the DA solution to exactly match the expected value computed by the MC model.

3.3 Optimization of optical properties in an adult atlas model

We repeat the above computation over the Colin27 atlas, and the error contour plots between the DA estimates (E_{gm}, Φ, S_{gm} and F_{gm}) at all combinations of μ_a and μ_s' values and the respective ground-truth values obtained using MC are plotted in Figs. 2(e)-2(h). Again, we only show the plots using optical properties at 830 nm as an example; those at 690 nm look similar and are not shown.

Comparing to the plots derived from the layered head model, we found a few notable differences. First, while the error plots for Φ and S_{gm} still present the zero-error contours; E_{gm} and

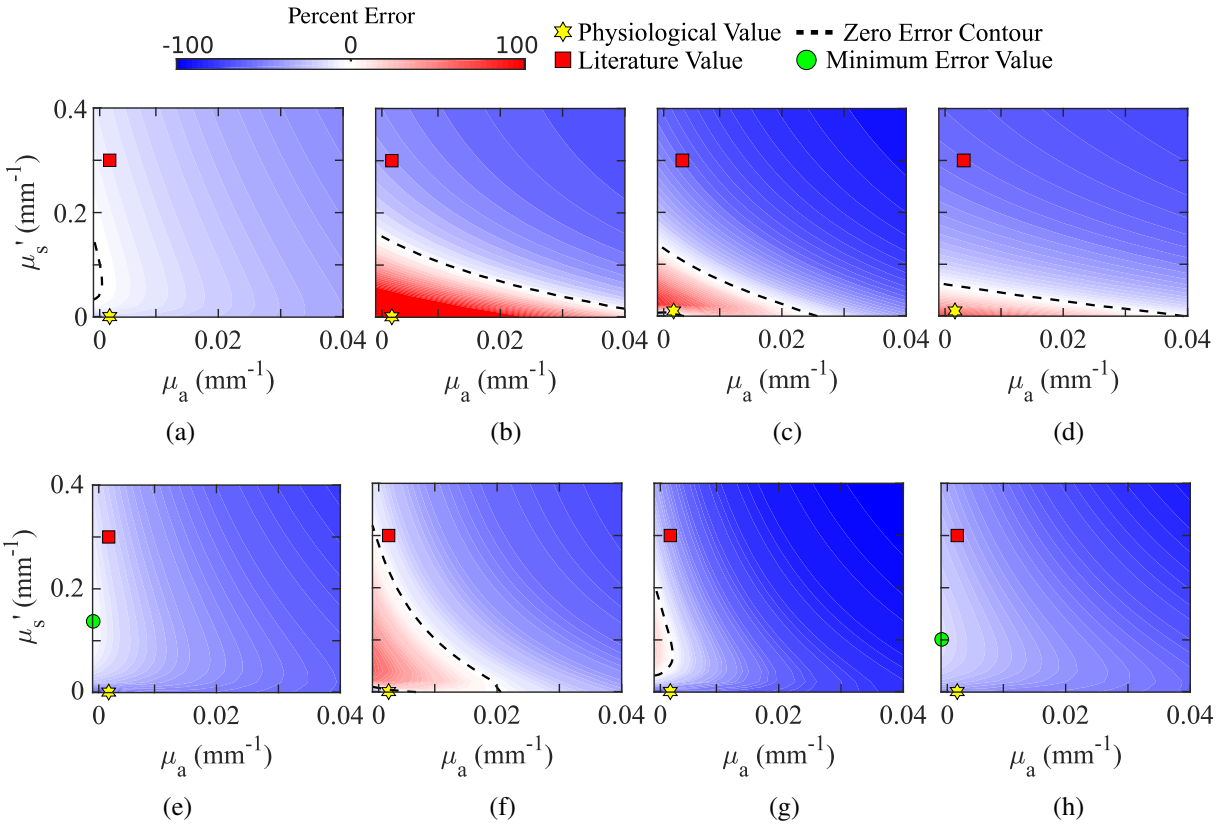

Fig 2 Error contour plots for DA computed at a range of CSF values compared to the MC reference solutions computed with CSF's physiological values ($\mu_a = 0.0026$ mm^{-1}, $\mu_s' = 0.001$ mm^{-1}) in a layered head model (a-d) and atlas model (e-h). We report (a, e) GM energy deposition (E_{gm}), (b, f) detector fluence (Φ) at 35 mm separation, (c, g) total GM sensitivity (S_{gm}) at 35 mm separation, and (d, h) fraction of GM sensitivity (F_{gm}) at 35 mm separation.

F_{gm} report underestimated estimates when using DA over all tested μ_a and μ_s' value combinations. In both cases, a minimal error property combination, marked by a green disk in Figs. 2(e) and 2(h) is computed for both of these metrics. Another notable difference is that the contour lines of the error surfaces for the 4 selected metrics show different shapes between the layered and atlas brain models, suggesting that the choice of brain anatomical models does have notable impact to forward solutions. Nonetheless, in both cases, the overall error surfaces from all tests demonstrate a smooth monotonic trend. The desired CSF equivalent optical properties that minimize the DA modeling errors, as either dashed line or green disks, can be readily identified from Fig. 2.

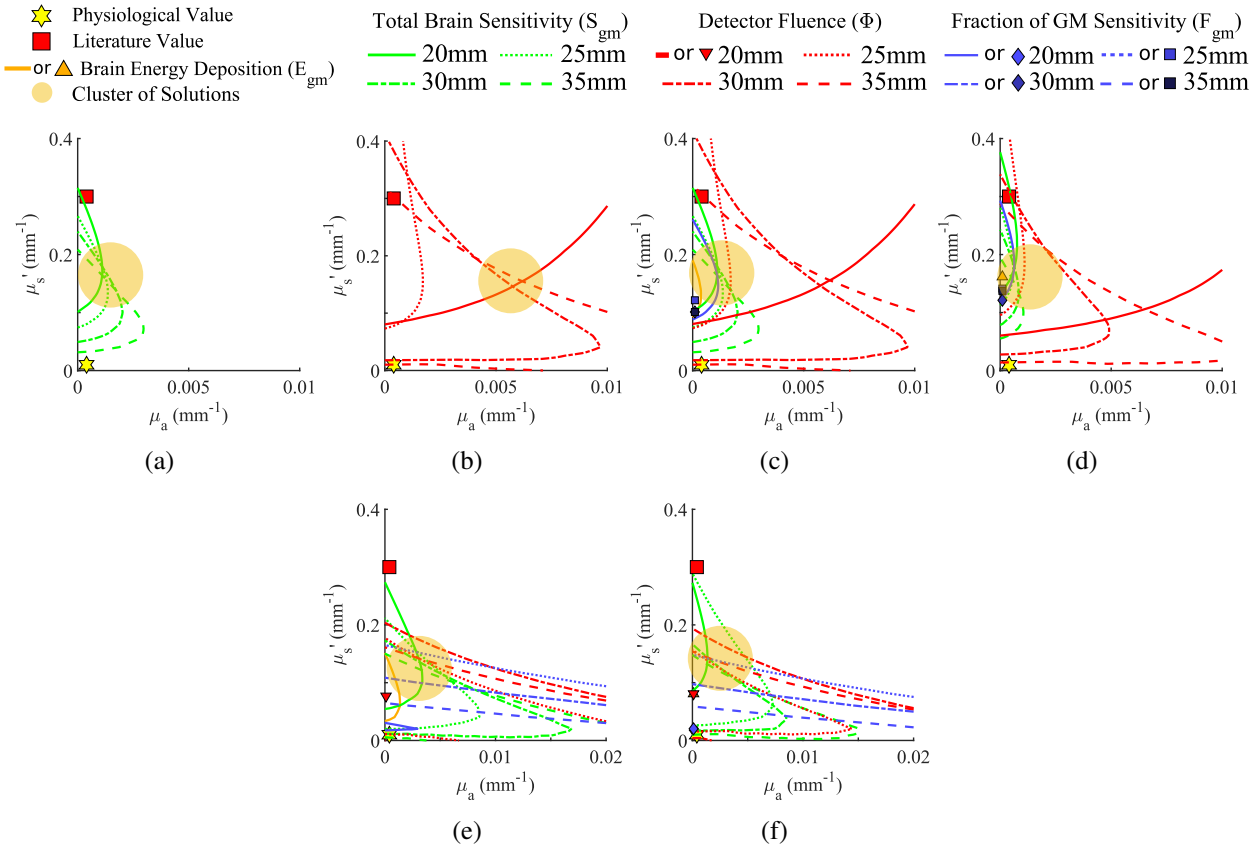

Fig 3 Aggregated zero-error contours and minimum error points for DA metrics computed at a range of CSF optical properties with MC as the reference solution. We show error minimization for GM sensitivity with an 830 nm source (a), detector fluence with an 830 nm source (b), and all metrics with 830 nm (c) and 690 nm (d) sources in the atlas model. In the layered-head model, we show error minimization of all metrics with an 830 nm source (e) and 690 nm source (f).

3.4 Simultaneously minimizing errors in two or more optical metrics

The results shown in Fig. 3 demonstrate that it is possible to completely eliminate or, in some cases, minimize modeling errors for a given metric when using DA in brain simulations by choosing a specific set of equivalent CSF optical properties. However, it is generally desirable to recommend a set of CSF equivalent optical properties that can simultaneously minimize two or more optical metrics. To achieve this goal, in Figs. 3(a)-3(b), we first show the overlay of the zero-error contour lines for S_{gm} and Φ, respectively, for the Colin27 atlas at 830 nm across 4 different separations to illustrate basic rationales when minimizing two metrics simultaneously. From Fig. 3(a), it appears that the zero-error contours for S_{gm} at various separations intersect each other in a compact region, indicated by a shaded circle. It is clear that the μ_a and μ_s' values at any intersection point of two zero-error contours is able to completely eliminate the DA modeling error for both separations. For example, $\mu_a = 0.00173$ mm^{-1} and $\mu_s' = 0.138$ mm^{-1} are the optimal CSF optical properties when one aims to minimize the error caused by DA for brain sensitivity at both 30 mm and 35 mm source-detector separations, with the 830 nm source. The μ_a and μ_s' values near the center of the cluster of the intersection points, roughly located at $\mu_a = 0.0026$ mm^{-1} and $\mu_s' = 0.14$ mm^{-1}, is suitable to minimize the error for all 4 tested source-detector separations despite that it can not eliminate the error like those values at the exact intersection points. Similar optimization can be made on the error contour plots for fluence measurements Φ shown in Fig. 3(b). In this case, the intersection points are less clustered than those for S_{gm}. Nonetheless, optimal CSF property settings can be found for every pair of separations.

To generalize our findings, in Figs. 3(a)-3(d), we overlay the zero-error contour lines computed from all tested metrics and source-detector separations. We show such collective zero-error contour

plots for both the 5-layer (c, e) and Colin27 atlas (d, f) at either 830 nm (c, d) or 690 nm (e, f). In these plots, red lines represent errors for Φ; green lines show the errors for S_{gm}, and blue lines show those for F_{gm}. When a zero-error contour is not found in the search space, a marker of the corresponding color is shown marking the μ_a and μ_s' values that minimize the error of the respective metric.

It is clear that there is no single solution that can simultaneously eliminate DA modeling errors in all metrics and separations. However, we would like to highlight some general observations, from which we attempt to offer an updated recommendation for the equivalent CSF optical properties in DA.

First of all, nearly all zero-error contour lines are located below the previously recommended values (red squares), suggesting that lowering the recommended μ_s' values could potentially reduce the overall modeling errors. Secondly, the brain sensitivity (S_{gm}, shown in green) generally shows a more clustered intersection distribution than other metrics, with the optimal μ_a value in the vicinity of the physiological μ_a value. Thirdly, simultaneously minimizing surface fluence (Φ) at multiple separations generally requires a larger μ_a value, but the μ_s' of these intersection points is comparable to those for minimizing errors of other metrics, which is about 1/2 to 1/3 of the literature recommendation. To better guide the interpretation of these findings, in Figs. 3(e)-3(d), we draw a yellow-shaded circle on each plot indicating the rough clustered location of the zero-error contours and their intersections.

Despite the fact that there is not a single μ_a and μ_s' combination that could minimize all metrics, we still feel strongly that recommending a single set of μ_a and μ_s' equivalent CSF properties is still quite helpful, especially considering the wide adoption the similar recommendation from Custo *et al.*. Consolidating our findings described above, we suggest to lower the μ_s' from the previously

recommended 0.3 mm^{-1} to 0.15 mm^{-1} while maintaining μ_a to match the respective physiological values.

3.5 Verification of error reduction at optimized CSF property values

To verify that the updated recommendation of CSF equivalent properties for DA can lead to significantly lower errors over the previously recommended values, we recomputed the fluence distributions and the Jacobians for a source-detector separation of 30 mm, similar to those shown in Figs. 4(a) and 4(c), using the updated recommendations and show side-by-side comparisons in Fig. 4 before and after this optimization. The spatial distributions of the DA (gray) and MC (white) solutions are indicated as contour lines (the closer the match, the better); the spatially-resolved percentage errors (the lower the better) of the fluence and Jacobian are also plotted as the color map in these plots.

From fluence and Jacobian distributions in both 5-layer and atlas models, the new recommendation significantly improves the match with the ground-truth MC solutions across the domain, with particularly notable improvement in the CSF, GM and WM layers. The error distributions in all plots also become significantly more uniform across the simulated domain while shifting towards the low-error end. The remaining mismatch between DA and MC largely aggregates in the CSF region, while the peak error is significantly lowered when using the new recommendation. It is worth highlighting that the mismatch within the GM region has been improved dramatically. Because the GM region is particularly important in fNIRS data analysis, our updated recommendation will likely result in enhanced fNIRS analysis accuracy.

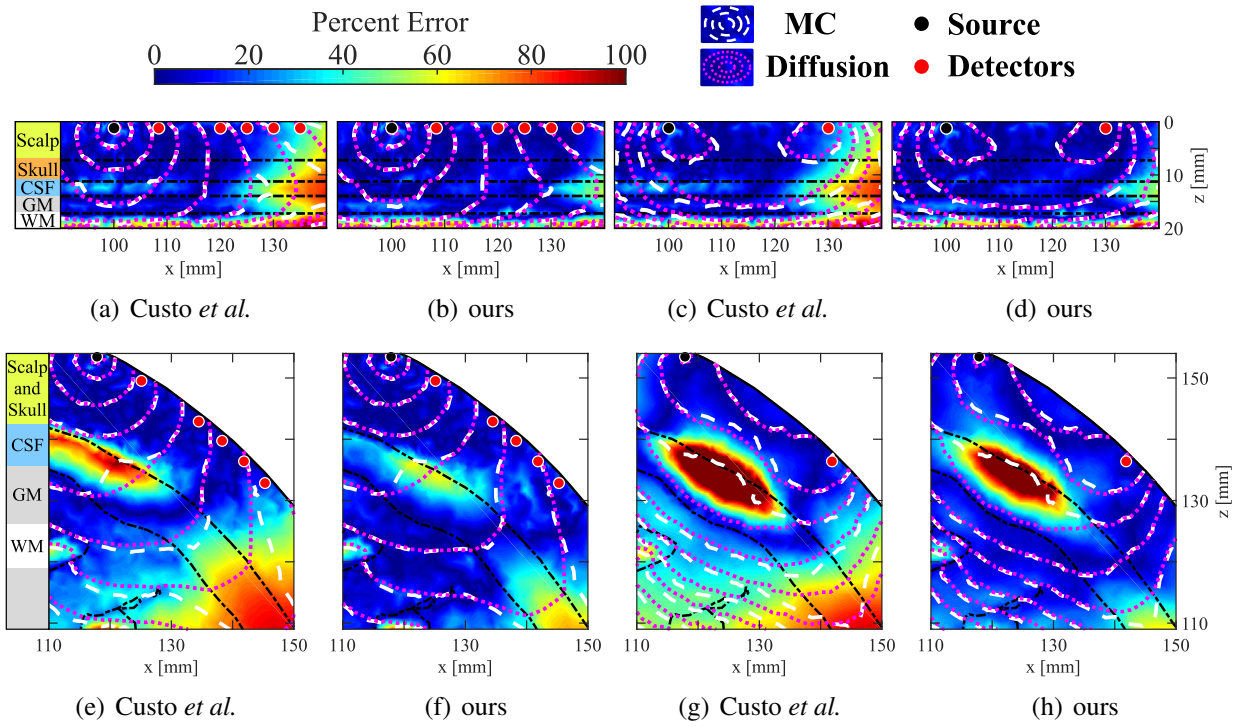

Fig 4 Cross sections of fluence and the 30 mm source-detector separation Jacobian in DA and MC models with a 830 nm source using previously recommended values ($\mu_a = 0.0026$ mm^{-1}, $\mu_s' = 0.3$ mm^{-1}) and our recommended values ($\mu_a = 0.0026$ mm^{-1}, $\mu_s' = 0.15$ mm^{-1}) with absolute error (color maps) and log-scale contours of DA (brown) and MC (white). We show a direct comparison for fluence (a, b) and sensitivity (c, d) for the layered head model, as well as fluence (e, f) and sensitivity (g, h) in the atlas model.

4 Discussions

To the best of our knowledge, this work represents the first systematic comparison between DA and MC in the handling of the low-scattering CSF tissues in brain/full-head light transport simulations. We focus on revisiting a set of equivalent CSF optical properties in DA based recommended by a widely cited work by Custo *et al.*, understanding its limitations and seeking to revise it to achieve improved modeling accuracy. Despite the relatively straightforward methodology, we believe that our updated recommendation for modeling CSF in DA is highly significant and could have a broad impact given the widespread use of the previously recommended CSF optical property values.

Based on the results presented in the above section, we want to highlight a number of key find-

ings. First, we demonstrate that in most of the investigated optical metrics, it is possible to exactly match DA with MC when a particular optical metric is of interest. As a matter of fact, in most tested metrics, there are an infinite number of such solutions. We believe that this is a result of the additional degree-of-freedom offered by allowing both μ_a and μ_s' to vary. In comparison, most previous works were focused on optimizing μ_s' only. Secondly, a unique combination of CSF μ_a and μ_s' often exists to simultaneously match DA with MC when two optical metrics are considered, indicated as the intersection between any pair of zero-error contours shown in Fig. 3. Thirdly, exactly matching DA with MC solutions at more than 2 optical metrics becomes impossible, however, clusters of intersection points of zero-error curves exist and could be utilized to minimize modeling errors for a specific subset of the desired metrics. Moreover, from Figs. 2 and 3, it is clear that the previously recommended CSF optical properties tend to underestimate nearly all tested metrics when used with DA. This is indicated by the blue-colored regions where the red-square markers are located in Fig. 2 and the fact that most zero-error contours shown in Fig. 3 are below the red-square markers along the y-axis. Finally, using the distributions of the zero-error contours from all metrics, we reduce these complex configurations into a simple updated recommendation: we recommend lowering the CSF equivalent μ_s' from 0.3 mm^{-1} in previous recommendation to 0.15 mm^{-1}, while keeping the absorption coefficient at the physiological value.

Another advance made through this work compared to previous works is the extension from only matching the surface fluence between DA and MC to a number of fNIRS/PBM relevant metrics, including total GM sensitivity (S_{gm}) and brain energy deposition (E_{gm}). On the one hand, the distinctive distributions of the zero-error contour plots for each of these metrics suggest that choosing different optical metrics to optimize could lead to different optimal CSF property settings. On the other hand, comparing to the previously recommended CSF optical properties, the optimal CSF

properties across various metrics all seem to require a lower μ_s' value. Similarly, our systematic benchmarks also extend the simulation domain from an atlas model in Custo *et al.* to also consider a layered brain model, which has also been frequently used in the literature.[21,31] While the error contour plots and zero-error curves show notable visual differences, the observations between both head models, as summarized above, are generally similar.

We recognize that there are a few limitations of this current study. First of all, our primary interest is to characterize the errors between DA with MC solutions under the influence of CSF optical properties, while assuming all other settings are identical – including the geometry of the tested brain model, the assumed optical properties of all other brain layers, even the discretization methods (i.e. meshes). One should understand that exploring variations of these other simulation assumptions, which is beyond the scope of this work, would result in different optimal CSF optical properties. However, one could apply the same methodology as presented here to optimize CSF settings for specific application needs. Secondly, the updated CSF optical properties with $\mu_s' = 0.15$ mm^{-1} and μ_a at the literature physiological value is a compromise between simplicity and desired accuracy. On the one hand, the widespread use of the the previous recommendation by Custo *et al.* clearly demonstrates the need for a simple and easy-to-use approximation. On the other hand, as shown in Figs. 2 and 3, minimizing various optical metrics is a complex problem and there is not a simple solution. Thirdly, the study reported here specifically focuses on minimizing the DA-to-MC errors in selected forward and reconstruction related metrics. Despite that our updated recommendation can yield a significant reduction in error, including complete elimination in many cases, whether such metric-wise improvement can also make a significant impact on fNIRS/PBM data analyses depends on the type of data analysis and application. In general, many fNIRS studies currently focus on relative changes between stimuli and baseline conditions. The

systematic modeling errors revealed in this work may be partially alleviated due to the use of ratiometric measurements. Regardless, for any application where the Custo *et al.* CSF DA properties were useful, the new recommendation should be readily applicable and is anticipated to achieve improved results. Finally, a recent work by Hirvi *et al.*[10] explored further refinement of CSF by separately modeling the nearly transparent CSF2 region in the inner brain and the remaining semi-diffusive CSF space. Here we limit our domain to 5-layer or Colin27 model with a single CSF region and leave the modeling of CSF2 for future works.

5 Conclusion

In summary, we have systematically revisited a widely adopted recommendation on CSF equivalent optical properties to enable fast DA modeling in fNIRS data analysis with improved accuracy. By directly comparing DA with reference solutions computed by mesh-based MC, we performed comprehensive characterizations of the errors between DA and MC across various fNIRS/PBM relevant metrics, including surface fluence (Φ), total GM energy deposition (E_{gm}), total GM sensitivity (S_{gm}) and brain sensitivity fraction (F_{gm}), at common source-detector separations across two brain models and two wavelengths. We demonstrated that by allowing simultaneous adjustments of μ_a and μ_s', one can exactly match many single metrics between DA and MC, with an infinite number of optimal solutions along the zero-error contours. Unique optimal μ_a and μ_s' value combinations also exist among many pairs of metrics, indicated by the intersection between the two respective zero-error contours. After reviewing the overall distributions of the zero-error contours and their intersections, we found that the previously recommended CSF properties tend to underestimate many of the fNIRS/PBM relevant metrics due to their relatively high μ_s' value and consequently higher attenuation.

To offer the community a convenient set of CSF optical properties for DA, we consolidated our findings across all combinations of the tested metrics, separations, brain models and wavelengths, and suggest a revised recommendation: one should set the CSF's equivalent μ_s' to 0.15 mm^{-1} and maintain μ_a at its physiological value. Compared with the previously suggested recommendation, we demonstrated that DA simulations using the revised recommendation not only significantly reduce the errors of particular fNIRS/PBM metrics, but also reduce the spatially resolved error throughout our anatomical models, especially in the GM region. In addition, we carefully described our computational protocol for this optimization; one could follow this protocol to re-derive optimal CSF properties if additional constraints arise. Given the widespread use of the previously recommended CSF properties, we anticipate that our updated recommendation could generate a broad impact and improve the accuracy of fNIRS data analysis.

Disclosures

No conflicts of interest, financial or otherwise, are declared by the authors.

Code, Data, and Materials Availability

Our open-source DA solver, Redbird-m can be accessed at https://github.com/fangq/redbird-m; our mesh-based MC solver can be accessed at https://github.com/fangq/mmc. The raw data describing relative error for all metrics and combinations of CSF μ_a and μ_s' is provided in https://neurojson.org/db/cotilab/CSF_Neurophotonics_2024.

Acknowledgments

This research is supported by National Institutes of Health (NIH) grants R01-GM114365, R01-EB026998, and U24-NS124027.

References

1 S. R. Arridge and J. C. Hebden, "Optical imaging in medicine: II. Modelling and reconstruction," *Physics in Medicine & Biology* **42**, 841 (1997).

2 C. Zhu and Q. Liu, "Review of Monte Carlo modeling of light transport in tissues," *Journal of Biomedical Optics* **18**, 050902 (2013). Publisher: SPIE.

3 D. A. Boas, J. P. Culver, J. J. Stott, *et al.*, "Three dimensional Monte Carlo code for photon migration through complex heterogeneous media including the adult human head," *Opt. Express* **10**, 159–170 (2002).

4 Q. Fang and S. Yan, "Graphics processing unit-accelerated mesh-based Monte Carlo photon transport simulations," *Journal of Biomedical Optics* **24**, 115002 (2019). Publisher: SPIE.

5 L. Wang, S. L. Jacques, and L. Zheng, "MCML—Monte Carlo modeling of light transport in multi-layered tissues," *Computer Methods and Programs in Biomedicine* **47**(2), 131–146 (1995).

6 Q. Fang and D. A. Boas, "Monte Carlo simulation of photon migration in 3D turbid media accelerated by graphics processing units," *Opt. Express* **17**, 20178–20190 (2009).

7 Q. Fang, "Mesh-based Monte Carlo method using fast ray-tracing in Plücker coordinates," *Biomedical Optics Express* **1**, 165 (2010).

8 S. Yan and Q. Fang, "Hybrid mesh and voxel based Monte Carlo algorithm for accurate and efficient photon transport modeling in complex bio-tissues," *Biomedical Optics Express* **11**, 6262–6270 (2020). Publisher: Optica Publishing Group.

9 Y. Yuan, S. Yan, and Q. Fang, "Light transport modeling in highly complex tissues using

the implicit mesh-based Monte Carlo algorithm," *Biomedical Optics Express* **12**, 147–161 (2021). Publisher: Optica Publishing Group.

10 P. Hirvi, T. Kuutela, Q. Fang, *et al.*, "Effects of atlas-based anatomy on modelled light transport in the neonatal head," *Physics in Medicine & Biology* **68**, 135019 (2023).

11 H. Dehghani, M. E. Eames, P. K. Yalavarthy, *et al.*, "Near infrared optical tomography using NIRFAST: Algorithm for numerical model and image reconstruction," *Communications in numerical methods in engineering* **25**, 711–732 (2008).

12 Q. Fang, S. A. Carp, J. Selb, *et al.*, "A multi-modality image reconstruction platform for diffuse optical tomography," in *Biomedical Optics (2008), paper BMD24*, BMD24, Optica Publishing Group (2008).

13 E. Okada, M. Firbank, M. Schweiger, *et al.*, "Theoretical and experimental investigation of near-infrared light propagation in a model of the adult head," *Applied Optics* **36**, 21–31 (1997). Publisher: Optica Publishing Group.

14 S. R. Arridge, M. Schweiger, M. Hiraoka, *et al.*, "A finite element approach for modeling photon transport in tissue," *Medical Physics* **20**(2), 299–309 (1993).

15 A. H. Hielscher, R. E. Alcouffe, and R. L. Barbour, "Comparison of finite-difference transport and diffusion calculations for photon migration in homogeneous and heterogeneous tissues," *Physics in Medicine & Biology* **43**, 1285 (1998).

16 Y. Fukui, Y. Ajichi, and E. Okada, "Monte Carlo prediction of near-infrared light propagation in realistic adult and neonatal head models," *Applied Optics* **42**, 2881–2887 (2003). Publisher: Optica Publishing Group.

17 H. Dehghani, S. R. Arridge, M. Schweiger, *et al.*, "Optical tomography in the presence of void regions," *JOSA A* **17**, 1659–1670 (2000). Publisher: Optica Publishing Group.

18 J. Heiskala, P. Hiltunen, and I. Nissilä, "Significance of background optical properties, time-resolved information and optode arrangement in diffuse optical imaging of term neonates," *Physics in Medicine & Biology* **54**, 535 (2009).

19 G. Strangman, M. A. Franceschini, and D. A. Boas, "Factors affecting the accuracy of near-infrared spectroscopy concentration calculations for focal changes in oxygenation parameters," *NeuroImage* **18**, 865–879 (2003).

20 A. Custo, W. M. Wells III, A. H. Barnett, *et al.*, "Effective scattering coefficient of the cerebral spinal fluid in adult head models for diffuse optical imaging," *Applied Optics* **45**, 4747 (2006).

21 E. Okada and D. T. Delpy, "Near-infrared light propagation in an adult head model. I. Modeling of low-level scattering in the cerebrospinal fluid layer," *Applied Optics* **42**, 2906–2914 (2003). Publisher: Optica Publishing Group.

22 P. Kochunov, J.-F. Mangin, T. Coyle, *et al.*, "Age-related morphology trends of cortical sulci," *Human Brain Mapping* **26**(3), 210–220 (2005). _eprint: https://onlinelibrary.wiley.com/doi/pdf/10.1002/hbm.20198.

23 A. Farina, A. Torricelli, I. Bargigia, *et al.*, "In-vivo multilaboratory investigation of the optical properties of the human head," *Biomedical Optics Express* **6**, 2609–2623 (2015). Publisher: Optica Publishing Group.

24 H. Dehghani, B. R. White, B. W. Zeff, *et al.*, "Depth sensitivity and image reconstruction analysis of dense imaging arrays for mapping brain function with diffuse optical tomography," *Applied Optics* **48**, D137–D143 (2009). Publisher: Optica Publishing Group.

25 A. T. Eggebrecht, B. R. White, S. L. Ferradal, *et al.*, "A quantitative spatial comparison of high-density diffuse optical tomography and fMRI cortical mapping," *NeuroImage* **61**, 1120–1128 (2012).

26 A. T. Eggebrecht and J. P. Culver, "NeuroDOT: An extensible Matlab toolbox for streamlined optical functional mapping," in *Diffuse Optical Spectroscopy and Imaging VII (2019), paper 11074_26*, 11074_26, Optica Publishing Group (2019).

27 Y. Zhan, A. T. Eggebrecht, J. P. Culver, *et al.*, "Image Quality Analysis of High-Density Diffuse Optical Tomography Incorporating a Subject-Specific Head Model," *Frontiers in Neuroenergetics* **4** (2012). Publisher: Frontiers.

28 J. Defenderfer, S. Forbes, S. Wijeakumar, *et al.*, "Frontotemporal activation differs between perception of simulated cochlear implant speech and speech in background noise: An image-based fNIRS study," *NeuroImage* **240**, 118385 (2021).

29 L. H. Collins-Jones, R. J. Cooper, C. Bulgarelli, *et al.*, "Longitudinal infant fNIRS channel-space analyses are robust to variability parameters at the group-level: An image reconstruction investigation," *NeuroImage* **237**, 118068 (2021).

30 C. J. Holmes, R. Hoge, L. Collins, *et al.*, "Enhancement of MR Images Using Registration for Signal Averaging," *Journal of Computer Assisted Tomography* **22**, 324 (1998).

31 A. P. Tran, S. Yan, and Q. Fang, "Improving model-based functional near-infrared spectroscopy analysis using mesh-based anatomical and light-transport models," *Neurophotonics* **7**, 015008 (2020). Publisher: SPIE.

32 A. N. Yaroslavsky, P. C. Schulze, I. V. Yaroslavsky, *et al.*, "Optical properties of selected

native and coagulated human brain tissues in vitro in the visible and near infrared spectral range," *Physics in Medicine & Biology* **47**, 2059 (2002).

33 M. M. Wu, S.-T. Chan, D. Mazumder, *et al.*, "Improved accuracy of cerebral blood flow quantification in the presence of systemic physiology cross-talk using multi-layer Monte Carlo modeling," *Neurophotonics* **8**, 015001 (2021). Publisher: SPIE.

34 R. Hochuli, S. Powell, S. Arridge, *et al.*, "Quantitative photoacoustic tomography using forward and adjoint Monte Carlo models of radiance," *Journal of Biomedical Optics* **21**, 126004 (2016). Publisher: SPIE.

35 M. Dehaes, P. E. Grant, D. D. Sliva, *et al.*, "Assessment of the frequency-domain multi-distance method to evaluate the brain optical properties: Monte Carlo simulations from neonate to adult," *Biomedical Optics Express* **2**, 552–567 (2011). Publisher: Optica Publishing Group.

36 S. Brigadoi, P. Aljabar, M. Kuklisova-Murgasova, *et al.*, "A 4D neonatal head model for diffuse optical imaging of pre-term to term infants," *NeuroImage* **100**, 385–394 (2014).

37 M. M. Wu, R. W. Horstmeyer, and S. A. Carp, "scatterBrains: an open database of human head models and companion optode locations for realistic Monte Carlo photon simulations," *Journal of Biomedical Optics* **28**, 100501 (2023). Publisher: SPIE.

38 M. M. Wu, K. Perdue, S.-T. Chan, *et al.*, "Complete head cerebral sensitivity mapping for diffuse correlation spectroscopy using subject-specific magnetic resonance imaging models," *Biomedical Optics Express* **13**, 1131–1151 (2022). Publisher: Optica Publishing Group.

39 Q. Fang, J. Selb, S. A. Carp, *et al.*, "Combined optical and x-ray tomosynthesis breast imaging," *Radiology* **258**(1), 89–97 (2011). PMID: 21062924.

40 Q. Fang, R. H. Moore, D. B. Kopans, *et al.*, "Compositional-prior-guided image reconstruction algorithm for multi-modality imaging," *Biomed. Opt. Express* **1**, 223–235 (2010).

41 B. Deng, D. H. Brooks, D. A. Boas, *et al.*, "Characterization of structural-prior guided optical tomography using realistic breast models derived from dual-energy x-ray mammography," *Biomed. Opt. Express* **6**, 2366–2379 (2015).

42 R. C. Haskell, L. O. Svaasand, T.-T. Tsay, *et al.*, "Boundary conditions for the diffusion equation in radiative transfer," *JOSA A* **11**, 2727–2741 (1994). Publisher: Optica Publishing Group.

43 E. Hernandez-Martin and J. L. Gonzalez-Mora, "Diffuse optical tomography in the human brain: A briefly review from the neurophysiology to its applications," *Brain Science Advances* **6**, 289–305 (2020). Publisher: SAGE Publications Ltd.

44 R. Yao, X. Intes, and Q. Fang, "Direct approach to compute Jacobians for diffuse optical tomography using perturbation Monte Carlo-based photon "replay"," *Biomedical Optics Express* **9**, 4588–4603 (2018). Publisher: Optica Publishing Group.

List of Figures

1 Comparison between diffusion approximation (DA) and Monte Carlo (MC) models in fluence distributions (contour lines) and percentage errors (color maps) in (a-c) a 5-layered head model and (d-f) the Colin27 atlas with a 830 nm source. The cerebrospinal fluid (CSF) optical properties are set to (a, d) a non-physiological diffusive medium of $\mu_a = 0.0026$ mm^{-1} and $\mu_s' = 1$ mm^{-1}, (b, e) the assumed physiological values of $\mu_a = 0.0026$ mm^{-1}, $\mu_s' = 0.001$ mm^{-1}, and (c, f) the literature recommended equivalent values for DA at $\mu_a = 0.0026$ mm^{-1} and $\mu_s' = 0.3$ mm^{-1}) while MC utilizes CSF's physiological values. 11

2 Error contour plots for DA computed at a range of CSF values compared to the MC reference solutions computed with CSF's physiological values ($\mu_a = 0.0026$ mm^{-1}, $\mu_s' = 0.001$ mm^{-1}) in a layered head model (a-d) and atlas model (e-h). We report (a, e) GM energy deposition (E_{gm}), (b, f) detector fluence (Φ) at 35 mm separation, (c, g) total GM sensitivity (S_{gm}) at 35 mm separation, and (d, h) fraction of GM sensitivity (F_{gm}) at 35 mm separation. 13

3 Aggregated zero-error contours and minimum error points for DA metrics computed at a range of CSF optical properties with MC as the reference solution. We show error minimization for GM sensitivity with an 830 nm source (a), detector fluence with an 830 nm source (b), and all metrics with 830 nm (c) and 690 nm (d) sources in the atlas model. In the layered-head model, we show error minimization of all metrics with an 830 nm source (e) and 690 nm source (f). 14

4 Cross sections of fluence and the 30 mm source-detector separation Jacobian in DA and MC models with a 830 nm source using previously recommended values ($\mu_a = 0.0026$ mm^{-1}, $\mu_s' = 0.3$ mm^{-1}) and our recommended values ($\mu_a = 0.0026$ mm^{-1}, $\mu_s' = 0.15$ mm^{-1}) with absolute error (color maps) and log-scale contours of DA (brown) and MC (white). We show a direct comparison for fluence (a, b) and sensitivity (c, d) for the layered head model, as well as fluence (e, f) and sensitivity (g, h) in the atlas model. 18

List of Tables

1 Assumed absorption (μ_a) and reduced scattering coefficients (μ_s'), both in mm^{-1}, based upon literature used to obtain the ground-truth results using Monte Carlo simulations. 6